Spatiotemporal dynamics of the covariant Lyapunov vectors of chaotic convection

M. Xu and M. R. Paul

The Spatiotemporal Dynamics of the Covariant Lyapunov Vectors of Chaotic Convection

M. Xu and M. R. Paul*

Department of Mechanical Engineering, Virginia Tech, Blacksburg, Virginia 24061

(Dated: March 14, 2018)

We explore the spatiotemporal dynamics of the spectrum of covariant Lyapunov vectors for chaotic Rayleigh-Bénard convection. We use the inverse participation ratio to quantify the amount of spatial localization of the covariant Lyapunov vectors. The covariant Lyapunov vectors are found to be spatially localized at times when the instantaneous covariant Lyapunov exponents are large. The spatial localization of the Lyapunov vectors often occurs near defect structures in the fluid flow field. There is an overall trend of decreasing spatial localization of the Lyapunov vectors with increasing index of the vector. The spatial localization of the covariant Lyapunov vectors with positive Lyapunov exponents decreases an order of magnitude faster with increasing vector index than all of the remaining vectors that we have computed. We find that a weighted covariant Lyapunov vector is useful for the visualization and interpretation of the significant connections between the Lyapunov vectors and the flow field patterns.

I. INTRODUCTION

The spatiotemporal dynamics of large extended systems that are driven far-from-equilibrium are at the center of many important problems of intense interest [1, 2]. Examples include the complex dynamics of the atmosphere and oceans [3], the dynamics of sunspots in the sun's photoshpere [4], the patterns of chemical reactions in cardiac tissue [5], the transition to turbulent fluid flow in a pipe [6–8], and the complex spatiotemporal patterns of social dynamics [9]. These problems are very difficult to understand because the systems are usually strongly nonlinear with very high-dimensional dynamics.

A powerful approach that can be used to build a physical understanding of these systems is based upon the use of covariant Lyapunov vectors [10–13]. For many years, the covariant Lyapunov vectors remained mostly a formal idea due to the lack of a tractable approach for their computation [10, 11]. However, efficient and scalable algorithms are now available [14–16].

There are new fundamental insights that can be gained by computing the covariant Lyapunov vectors for fluid systems. An important example is the computation of the principal angle between the stable and unstable manifolds. In the following, we will assume the Lyapunov exponents are ordered in the usual manner from largest to smallest and that there is a corresponding Lyapunov vector associated with each Lyapunov exponent.

The covariant Lyapunov vectors with positive Lyapunov exponents span the unstable manifold and the covariant Lyapunov vectors with negative Lyapunov exponents span the stable manifold. The principal angle is the minimum angle between the linear combination of the vectors spanning the unstable and stable manifolds. The principal angle therefore describes the degree of hyperbolicity of the dynamics [14, 17].

If the principal angle is bounded away from zero, the dynamics are hyperbolic. In this case, the unstable and stable manifolds never become nearly tangent with one another. Otherwise, if the principal angle is not bounded away from zero, the dynamics are non-hyperbolic and the unstable and stable manifolds experience moments of near tangency. Many important theorems of dynamical systems theory, such as the shadowing theorem, rest upon the assumption of hyperbolic dynamics [18–20]. For example, this idea was used to study the transition between hyperbolic and non-hyperbolic dynamics for chaotic Kolmogorov flow as the Reynolds number was increased [21].

The hyperbolic properties of the covariant Lyapunov vectors have also been used to decompose the dynamics of a number of model systems into two different classes of modes called the physical modes and spurious modes (also called transient modes) [17, 22–24]. The model systems have included coupled-map lattices, the complex Ginzburg-Landau equation, and the Kuramoto-Sivashinsky equation [17, 22–24].

The physical modes are characterized by covariant Lyapunov vectors with frequent near tangencies with one another in the tangent space. These are found to include all of the Lyapunov vectors with positive Lyapunov exponents and also some of the Lyapunov vectors with negative Lyapunov exponents. All of the remaining Lyapunov vectors were found to be hyperbolically isolated from one another and are the spurious modes.

It has been argued that the physical modes contain the essential information, or the number of effective degrees of freedom, needed to describe the dynamics and that the spurious modes are numerical artifacts arising from excess resolution in the computation [17]. This is an exciting and powerful idea, especially if it can be found to also apply to experimentally accessible fluid systems governed by the Navier-Stokes equations.

The number of physical modes have been found to be extensive and it has been suggested that the number of physical modes are related to the dimension of the inertial manifold [17, 23, 24]. It is interesting to note, that the

estimate for the dimension of the inertial manifold is typically several times larger than the value of the Kaplan-Yorke dimension (also called the fractal dimension) for the same dynamics [17, 23, 24]. Ding *et al.* [24, 25] computed the dimension of the inertial manifold six different ways using unstable periodic orbit theory and found that all of the computations agree with the estimate found using the number of physical modes.

The covariant Lyapunov vectors of chaotic Rayleigh-Bénard convection have been computed [26]. The covariant Lyapunov vectors with positive, zero, and small negative Lyapunov exponents were found to be spatially localized near small-scale defect structures in the flow field. In particular, the magnitude of the covariant Lyapunov vectors were large near roll pinch-off and roll merger events as well as near wall-foci. These findings extend the idea of localized Lyapunov vectors beyond that of the leading order Lyapunov vector which was found in previous studies of chaotic Rayleigh-Bénard convection [27–31].

The chaotic dynamics were found to be non-hyperbolic for all of the Rayleigh numbers explored in Ref. [26]. An interesting result of this study was that *all* of the covariant Lyapunov vectors were tangled with their nearest neighbors. In other words, the leading order Lyapunov vector was highly tangled with the second Lyapunov vector and so on, all the way to the 141 Lyapunov vectors that were computed. There was no particular physical significance in choosing to compute 141 Lyapunov vectors other than the availability of computing resources and that this value is several times larger than the value of the fractal dimension for all of the parameters explored in Ref. [26]. The Lyapunov vectors were tangled in the sense that neighboring vectors had frequent near tangencies in the tangent space. In this case the Lyapunov vectors are coupled with one another, a small perturbation in the direction of one Lyapunov vector could affect the dynamics of its neighbors and so on.

In light of this, it was not possible to decompose the chaotic dynamics into physical and spurious modes using the ideas of [17]. However, it is possible that this decomposition is still present but that it was not uncovered in these calculations. For example, it is possible that for the Boussinesq equations the splitting of the tangent space into physical and spurious modes requires more covariant Lyapunov vectors than what was accessible computationally. Another possibility is that these dynamics are affected by the boundary and geometry of the domain, which could complicate this possible decomposition due to finite-size effects.

These remain important and open questions of current interest. In this paper, we are not able to answer the questions about possibly decomposing the dynamics by computing even more Lyapunov vectors. Rather, we focus our attention upon the first 141 Lyapunov vectors and carefully quantify their spatiotemporal dynamics in an effort to distill out the physical insights present in this rich description of the dynamics. In particular, we will conduct our investigation for the dynamics and parameters used in Ref. [26].

The outline of our presentation is as follows. In §II we discuss Rayleigh-Bénard convection and the approach used in the computation of the covariant Lyapunov vectors. In §III we discuss our numerical results and quantify the spatiotemporal dynamics of the spectrum of covariant Lyapunov vectors. Lastly, in §IV we present some concluding remarks.

II. APPROACH

Rayleigh-Bénard convection occurs when a shallow layer of fluid is heated from below in a gravitational field [1, 32]. Our conventions are defined in Fig. 1. The equations governing convection are the Boussinesq equations

$$\sigma^{-1}(\partial_t + \vec{u} \cdot \nabla)\vec{u} = -\nabla p + \nabla^2 \vec{u} + RT\vec{z} \qquad (1)$$
$$(\partial_t + \vec{u} \cdot \nabla)T = \nabla^2 T \qquad (2)$$
$$\nabla \cdot \vec{u} = 0. \qquad (3)$$

where $\vec{u}$ is the fluid velocity vector, T is the temperature, p is the pressure, ∂_t is a time derivative and $\vec{z}$ is a unit vector in the z-direction opposing gravity.
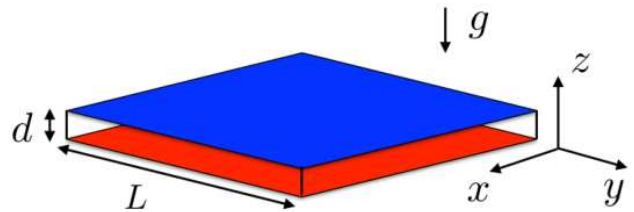

FIG. 1. (color online) A schematic of the square planform convection domain used in our numerical simulations and our convention for the Cartesian coordinates (x, y, z). The aspect ratio of the domain is $\Gamma = L/d$ where L is the side length and d and is the layer depth. A shallow layer of fluid is contained between a hot surface (bottom, red) and a cold surface (top, blue) which are held at constant temperature. All material surfaces are no-slip and the lateral sidewalls are perfectly insulating. The direction of gravity g is vertically downward.

Equations (1)-(3) have been nondimensionalized in the typical manner [33] using the depth d of the fluid layer as the length scale, the vertical diffusion time of heat d^2/α for the time scale where α is the thermal diffusivity, and the constant temperature difference between the bottom and top surfaces as the temperature scale. We have used no-slip $\vec{u} = 0$ boundaries on all material walls that bound the fluid layer which include the bottom, top, and all sidewalls. The bottom surface is hot $T(z=0) = 1$, the top surface is cold $T(z=1) = 0$, and the lateral sidewalls are perfectly insulating which can be expressed as $\nabla \cdot T\hat{n} = 0$ where $\hat{n}$ is an outward pointing unit normal.

The dynamics of Rayleigh-Bénard convection are determined by the three nondimensional parameters R, σ,

and Γ. The Rayleigh number R is the ratio of buoyancy forces to viscous and thermal dissipation. The critical value $R_c = 1707.76$ indicates the onset of convection in an infinite fluid layer [34]. The Prandtl number σ is the ratio of the diffusivities for momentum and heat where $\sigma \approx 1$ for typical convection experiments using compressed gases [32, 35]. Lastly, the aspect ratio of the convection domain $\Gamma = L/d$ quantifies the spatial extent of the domain where L is a characteristic length. For our simulations in a square planform container, L is the side length of the domain as shown in Fig. 1.

In order to compute the covariant Lyapunov vectors we follow the approach described in Ref. [26] which uses the algorithm introduced by Ginelli *et al.* [14]. In the following, we provide only the essential details of the computational approach and we refer the reader to Ref. [26] for a more detailed description.

We compute N_λ covariant Lyapunov vectors and N_λ covariant Lyapunov exponents by numerically solving Eqs. (1)-(3) simultaneously with N_λ copies of the Boussinesq equations that have been linearized about the nonlinear trajectory in state space. These linearized equations, or tangent-space equations, can be expressed as

$$\sigma^{-1}(\partial_t \delta \vec{u}^{(i)} + \vec{u} \cdot \nabla \delta \vec{u}^{(i)} + \delta \vec{u}^{(i)} \cdot \nabla \vec{u}) = -\nabla \delta p^{(i)} \quad (4)$$
$$+ \nabla^2 \delta \vec{u}^{(i)} + R \delta T^{(i)} \vec{z}$$
$$\partial_t \delta T^{(i)} + \vec{u} \cdot \nabla \delta T^{(i)} + \delta \vec{u}^{(i)} \cdot \nabla T = \nabla^2 \delta T^{(i)} \quad (5)$$
$$\nabla \cdot \delta \vec{u}^{(i)} = 0 \quad (6)$$

where $i = 1, 2, \ldots, N_\lambda$.

In our notation, $\delta \vec{u}^{(i)}$, $\delta T^{(i)}$, and $\delta p^{(i)}$ are the ith perturbations of the velocity, temperature, and pressure, respectively. The no-slip boundary condition yields $\delta \vec{u}^{(i)} = 0$ at all material walls. The boundary conditions for the bottom and top surfaces are $\delta T^{(i)}(z=0) = T^{(i)}(z=1) = 0$ and at the insulating lateral sidewalls $\nabla \cdot \delta T^{(i)} \hat{n} = 0$.

The essential idea is to integrate Eqs. (1)-(3) and N_λ copies of Eqs. (4)-(6) forward in time while periodically performing and storing the results of a QR-decomposition of the linearized equations. This QR-decomposition results in sets of orthonormal Gram-Schmidt vectors $\{\vec{g}_n^{(i)}\}$ for $i = 1, 2, \ldots, N_\lambda$ that have been computed and stored at discrete times t_n. Next, in order to compute the covariant Lyapunov vector $\vec{\xi}^{(i)}$, an arbitrary vector $\vec{\zeta}^{(i)}$ is chosen that spans the subspace spanned by the Gram-Schmidt vectors which is then evolved *backwards* in time using the algorithm of Ref. [14]. As this backward time integration proceeds the vector $\vec{\zeta}^{(i)}$ will converge to the covariant Lyapunov vector $\vec{\xi}^{(i)}$.

Our computational approach is based upon the finite-difference Boussinesq solver developed by Chiam *et al.* [36]. We have used this approach as the basis for our parallel solver for the covariant Lyapunov vectors of convection. More details about the numerical approach can be found in Ref. [26].

In our calculations, the covariant Lyapunov vector $\vec{\xi}(i)$ is a very large vector with $4N$ elements where N is the number of spatial grid points used to represent the flow field. We can represent the covariant Lyapunov vector as the large column vector given by $\vec{\xi}^{(i)} = [\delta u^{(i)} \ \delta v^{(i)} \ \delta w^{(i)} \ \delta T^{(i)}]^T$ where $(\delta u^{(i)}, \delta v^{(i)}, \delta w^{(i)})$ are the ith components of the perturbation velocity in the (x, y, z) directions, respectively. The superscript T indicates a transpose such that this represents a column vector. The perturbation pressure $\delta p^{(i)}$ is not included because the pressure is not an independent dynamic variable for incompressible fluid dynamics.

The spectrum of covariant Lyapunov exponents λ_i is given by the infinite-time average

$$\lambda_i = \lim_{t \to \infty} \frac{1}{t} \ln \left(\frac{||\vec{\xi}^{(i)}(t)||}{||\vec{\xi}^{(i)}(0)||} \right) \quad (7)$$

for $i = 1, 2, \ldots, N_\lambda$. We will also find it useful to define the finite-time or instantaneous covariant Lyapunov exponents $\tilde{\lambda}_i(t)$ by

$$\tilde{\lambda}_i(t) = \frac{1}{t_0} \ln \left(\frac{||\vec{\xi}^{(i)}(t + t_0)||}{||\vec{\xi}^{(i)}(t_0)||} \right) \quad (8)$$

where t_0 is a finite interval of time. The infinite-time average (or long-time average in a numerical simulation) of $\tilde{\lambda}_i$ is the Lyapunov exponent λ_i.

The instantaneous Lyapunov exponent is useful by indicating the exponential growth or decay that occurred during that time interval t_0 which can be used to connect with the flow field or other spatiotemporal features of the dynamics. An important property of the the instantaneous Lyapunov exponents $\tilde{\lambda}_i$ is that their values fluctuate in time and, as a result, they are not guaranteed to always maintain the ordering of decreasing value with increasing index i. In the results we present for $\tilde{\lambda}_i$ we have used $t_0 = \Delta t$ where Δt is the time step used in the numerical integration of the Boussinesq equations.

It is important to point out that the instantaneous covariant Lyapunov exponents are *different* than the instantaneous Lyapunov exponents computed using the typical Gram-Schmidt approach although the long-time average of each converges to the correct value for λ_i [23]. The instantaneous covariant Lyapunov exponents are physically relevant through their direct connection with the covariant Lyapunov vectors. In all of our analysis that follows we have used the instantaneous covariant Lyapunov exponents.

The set of covariant Lyapunov vectors $\{\vec{\xi}^{(i)}\}$ are covariant in the sense that if they are integrated forward in time using the linearized equations, the vectors will grow or decay with an exponent λ_i and if they are integrated backward in time they will grow or decay with the exponent $-\lambda_i$ (where growth or decay depends upon the sign of the particular Lyapunov exponent).

In an effort to avoid any confusion with the definitions of forward, backward, and covariant Lyapunov

based diagnostics that can be found in the literature (c.f. [13, 15, 37] for discussions of the different definitions), all of the results in this paper are based upon the covariant Lyapunov vectors. Therefore, in our discussion that follows, unless stated otherwise, we will use Lyapunov vector and instantaneous Lyapunov exponent to refer to the covariant Lyapunov vector and instantaneous covariant Lyapunov exponent, respectively.

III. RESULTS AND DISCUSSION

We explore the spectrum of covariant Lyapunov vectors and exponents for chaotic convection in a square planform container with an aspect ratio of $\Gamma = 16$, Prandtl number $\sigma = 1$, and for Rayleigh numbers $5000 \leq R \leq 9000$.

Chaotic convection at these parameters was investigated in Ref. [26] where it was found that the dynamics were non-hyperbolic and all of the computed Lyapunov vectors were tangled with their neighbors. In addition, the Lyapunov vectors were found to be localized near defect structures and a checkered pattern emerged for the Lyapunov vectors with large negative Lyapunov exponents. Overall, a decomposition of the dynamics into physical modes and transient modes was not found. In this paper, we explore these dynamics further by quantifying the spatiotemporal features of the Lyapunov vectors for these conditions.

Figure 2 shows an image of a typical chaotic flow field from our numerical simulations for $R = 5000$. The image shows the temperature field at the horizontal mid-plane ($z = 1/2$) where red is hot rising fluid and blue is cool falling fluid. The fractal dimension of the chaotic dynamics at these parameters is $D_\lambda \approx 25$ [26].

In all of our computations we use an evenly spaced grid with $\Delta x = \Delta y = \Delta z = 1/8$ and a uniform time step $\Delta t = 1 \times 10^{-3}$. This results in a grid with $N = n_x \times n_y \times n_z = 129 \times 129 \times 9$ where (n_x, n_y, n_z) are the number of grid points in each direction. The total number of grid points is $N = 149,769$ and each Lyapunov vector can be represented as a large column vector with $4N = 599,076$ elements.

In our calculations we have computed $N_\lambda = 141$ covariant Lyapunov vectors at each value of the Rayleigh number. This represents a significant increase in the amount of data we have to describe the dynamics when compared with the flow field data alone. A significant challenge, that we explore here, is to explore how to visualize this large amount of data and to determine what new insights this can provide.

A. Visualizing covariant Lyapunov vectors

An important question is: How do we visualize and quantify the spatiotemporal dynamics of 141 of these $\sim 6 \times 10^5$ dimensional Lyapunov vectors to gain further
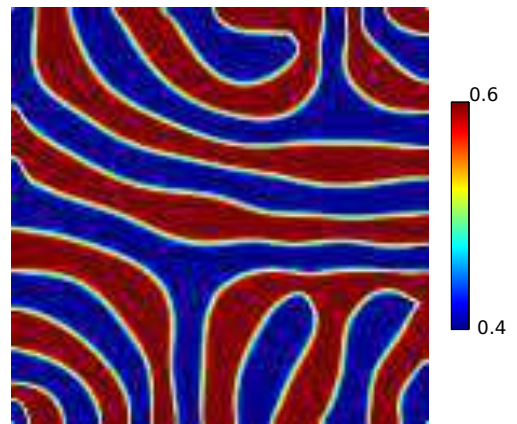

FIG. 2. (color online) An image of a typical flow field from a numerical simulation of chaotic convection. The temperature is shown at the mid-plane $T(x, y, z = 1/2, t)$ where red is hot rising fluid and blue is cool falling fluid. The color bar defines the scale used in the plot. ($R = 5000, \sigma = 1, \Gamma = 16$)

insight into the chaotic dynamics? In nearly all of the previous work on chaotic convection, the leading order Lyapunov vector has been visualized by viewing a spatial slice of only part of the vector [26–31]. In the following, we investigate this further and with the additional concern of how to visualize the entire spectrum of Lyapunov vectors.

It is attractive to represent the Lyapunov vectors using the spatial geometry of the physical domain in order to arrange the elements of the Lyapunov vector. This allows one to connect spatial features of the Lyapunov vectors with the spatial features of the flow field.

Figure 3 shows four different projections of this type for the leading order Lyapunov vector, at the horizontal mid-plane slice at $z = 1/2$, for the flow field shown in Fig. 2. Figure 3(a) shows the perturbation temperature field $\delta T^{(1)}$ and panels (b)-(d) illustrate the three components of the perturbation velocity $\delta u^{(1)}$, $\delta v^{(1)}$, and $\delta w^{(1)}$, respectively. Red indicates a large positive magnitude and blue indicates large negative magnitude. Therefore both red and blue represent regions of rapid growth and green represents regions of little growth. The black solid lines indicate the boundaries of the convection rolls for reference.

Figure 3(a)-(d) shows that the spatial variation of $\delta T^{(1)}$ and $\delta w^{(1)}$ are very similar which is expected for buoyancy driven flow. However, it is interesting that the perturbation velocities $\delta u^{(1)}$ and $\delta v^{(1)}$ also exhibit the same general trends. In addition, the magnitudes of the different perturbation fields in these images are all of the same order of magnitude. These results suggest that the temperature perturbation field at the horizontal mid-plane is a good representation of the Lyapunov vector.
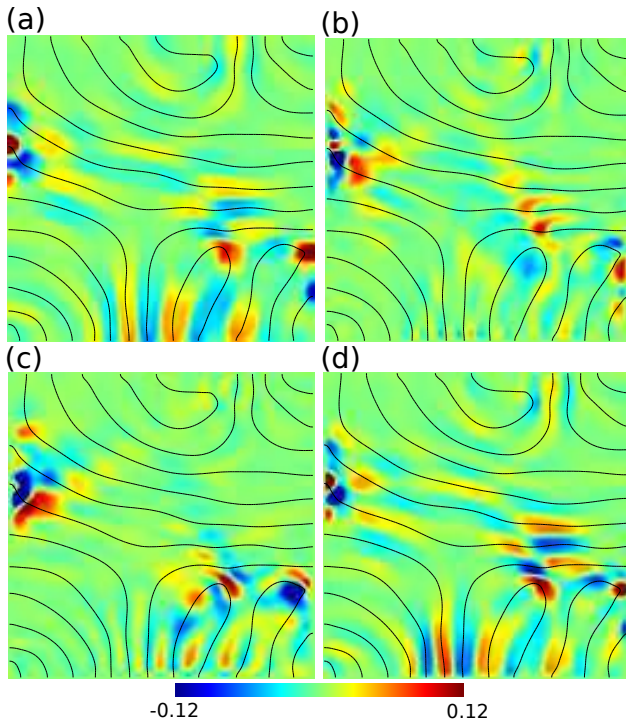
Before proceeding, we briefly discuss how this repre-

FIG. 3. (color online) Different projections of the leading order Lyapunov vector for the conditions of Fig. 2. Color contours indicate the value of the different perturbation fields at the horizontal mid-plane ($z = 1/2$) where red is a large positive value and blue is a large negative value. The black solid lines indicate the location of the convection rolls for reference. (a) Perturbation temperature $\delta T^{(1)}$, (b) perturbation velocity in the x-direction $\delta u^{(1)}$, (c) perturbation velocity in the y-direction $\delta v^{(1)}$, and (d) perturbation velocity in the z-direction $\delta w^{(1)}$.

sentation varied using horizontal slices at different values of the vertical position z. The spatial variation of the Lyapunov vector in the z-direction was found not to be significant and that a mid-plane slice is indeed a good representation of the Lyapunov vector. For example, the images of Fig. 3 are very similar at all values of z with some attenuation as one approaches the solid walls at either $z = 0$ or $z = 1$ (results not shown). We have confirmed that this is the case for the entire spectrum of Lyapunov vectors.

Lastly, we compare the perturbation temperature field with the complete Lyapunov vector at the horizontal mid-plane. Figure 4 shows the absolute value of the temperature perturbation in the first column and the magnitude of the entire Lyapunov vector in the second column for 3 different Lyapunov vectors of interest for $R = 5000$. Panels (a)-(b) are for the leading order Lyapunov vector and represents the most rapidly growing vector. Panels (c)-(d) are for the 12th Lyapunov vector which corresponds to the Lyapunov exponent closest to zero in our calculations. Finally, panels (e)-(f) are for the 141st Lyapunov vector which represents the most rapidly con-

tracting Lyapunov vector we have calculated.

We have calculated the magnitude of Lyapunov vector i using

$$||\vec{\xi}^{(i)}|| = \left(\delta u^{(i)^2} + \delta v^{(i)^2} + \delta w^{(i)^2} + \delta T^{(i)^2} \right)^{1/2} \quad (9)$$

which is evaluated at the horizontal mid-plane $||\vec{\xi}^{(i)}(x, y, z = 1/2, t)||$ to generate contour plots for comparison. Red represents a large magnitude and blue represents a small magnitude. Therefore, in Fig. 4 red regions represent locations of large growth and blue regions represent locations where there is very little growth.

The agreement between the two different representations of the Lyapunov vector in Fig. 4 is very good. This is true for all of the Lyapunov vectors in the spectrum that we computed although we only show three representative examples here. This suggests that the temperature perturbation field at the mid-plane captures the significant spatial features of the Lyapunov vector.

By using only the temperature perturbation component at the mid-plane this reduces the dimension of the plotted vector to $129 \times 129 = 16,641$. Although this is still quite large, it is smaller than the dimension of the full Lyapunov vector by a factor of $4n_z$ and is a significant reduction. In the following we will use the mid-plane slice of the perturbation temperature field to explore the spatial variation of the spectrum of Lyapunov vectors.

B.   Localization

A feature that consistently emerges in images such as those shown in Figs. (3)-(4) is the spatial localization of the Lyapunov vectors. Using our nondimensionalization, the width of a convection roll (for example, as measured by the distance between the black lines in Figs. 3-4) is approximately unity. This indicates that the length scale of the local regions of large growth have a length scale of approximately unity as well.

We are interested in quantifying this localization and its variation for the spectrum of Lyapunov vectors. Figure 5 illustrates how the spatial variation of the leading order Lyapunov vector can vary in time. Figure 5(a) shows an instance of time where the Lyapunov vector is highly localized near the center of the domain. Figure 5(b) illustrates the same Lyapunov vector twenty time-units later. At this later time, the spatial variation of the Lyapunov vector has changed significantly and it is now much more spatially distributed.

In order to quantify the spatial features of the Lyapunov vector we will use the inverse participation ratio [14, 38]. For our purposes we will define the inverse participation ratio, or localization, of Lyapunov vector i at time t as

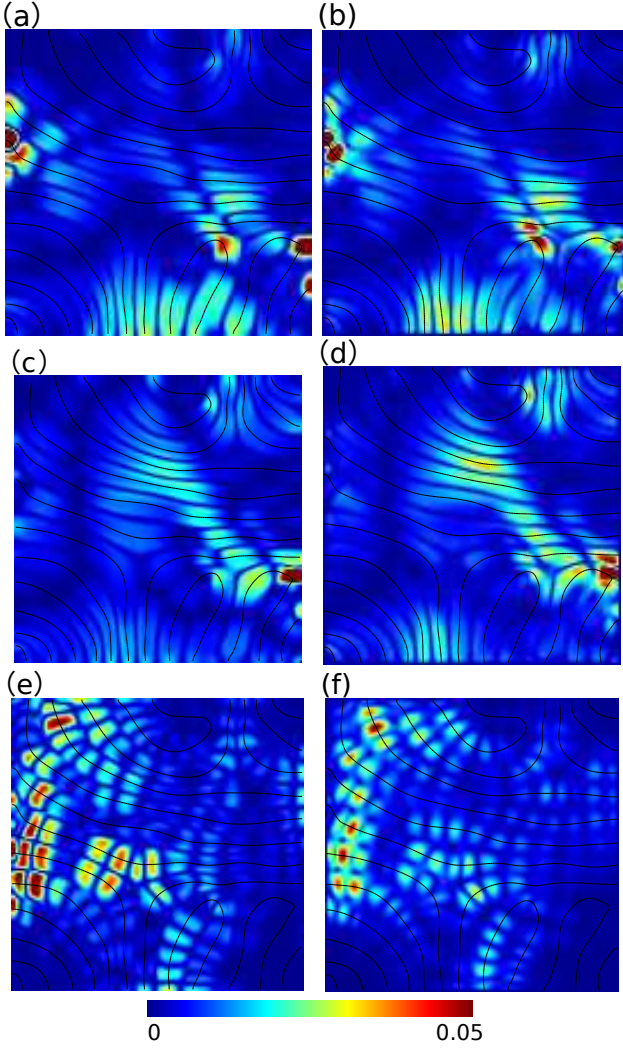$$C_i(t) = \sum_{x,y} \delta\tilde{T}^{(i)}(x, y, z = 1/2, t)^4 \quad (10)$$

FIG. 4. (color online) Comparison of the temperature perturbation field $|\delta T^{(i)}|$ and the magnitude of the Lyapunov vector $||\vec{\xi}^{(i)}||$ using Eq. (9) for the leading order Lyapunov vector ($i = 1$), the Lyapunov vector with a vanishing Lyapunov exponent ($i = 12$), and a rapidly decaying Lyapunov vector ($i = 141$). Color contours indicate the value of the different fields at the horizontal mid-plane ($z = 1/2$) where red is a large value and blue is small value. The black solid lines indicate the location of the convection rolls for reference. (a) $|\delta T^{(1)}|$, (b) $||\vec{\xi}^{(1)}||$, (c) $|\delta T^{(12)}|$, (d) $||\vec{\xi}^{(12)}||$, (e) $|\delta T^{(141)}|$, and (f) $||\vec{\xi}^{(141)}||$.

where the sum is again over all x and y at $z = 1/2$. The temperature perturbation field $\delta \tilde{T}^{(i)}$ has been normalized such that

$$\sum_{x,y} \delta \tilde{T}^{(i)}(x, y, z = 1/2, t)^2 = 1. \qquad (11)$$

The inverse participation ratio is a global indicator that we will use to quantify the spatial localization of the Lyapunov vectors. For the image shown in Fig. 5(a)
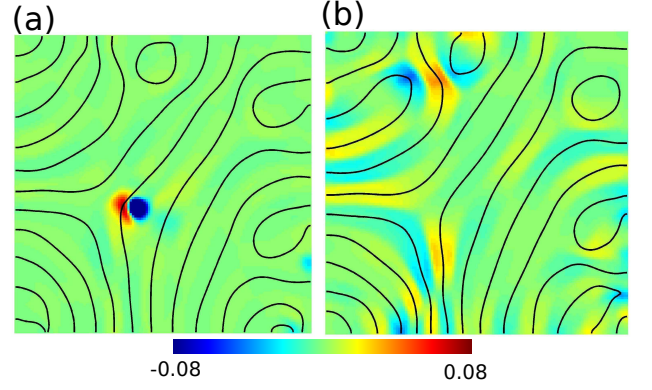

FIG. 5. (color online) The spatial variation of the leading order Lyapunov vector for $R = 5000$, $\sigma = 1$ and $\Gamma = 16$ at two different times. Color contours indicate the value of the perturbation temperature field $\delta T^{(1)}$ at the horizontal mid-plane ($z = 1/2$) where red is a large positive value and blue is a large negative value. The black solid lines indicate the location of the convection rolls for reference. (a) At this time the localization is large and $C_1 = 0.11$. This is reflected by the spatial distribution of the vector where its magnitude is mostly concentrated in one region near the center. (b) Twenty time units later the same Lyapunov vector is quite delocalized. At this time, C_1 is two orders of magnitude smaller at $C_1 = 0.001$.

the localization is $C_1 = 0.11$ whereas in panel (b) the localization is two orders of magnitude smaller at $C_1(t) = 0.001$.

By definition, the localization does not guarantee that this trend always be the case. For example, one could take the Lyapunov vector image shown in Fig. 5(a) and randomly shuffle the data points representing the red and blue regions in space and the resulting image would, of course, yield the precise same value for $C_i(t)$. However, in all of our explorations we have always found that $C_i(t)$ is large when the Lyapunov vector is spatially localized and that $C_i(t)$ is small when it is not as shown in Fig. 5. As a result, we will use $C_i(t)$ as a single scalar quantity to quantify the spatial localization of the Lyapunov vector as a function of time.

We now use C_i to explore the spatial features of the spectrum of Lyapunov vectors. In Fig. 6 we present results for the leading order Lyapunov vector. Figure 6(a) shows the time variation of the instantaneous Lyapunov exponent $\tilde{\lambda}_1$ given by Eq. (8), panel (b) shows the time variation of the localization $C_1(t)$, and panels (c)-(d) illustrate two representative images of the Lyapunov vector at times of interest.

Figure 6 illustrates that the leading order Lyapunov vector is spatially localized when the leading order Lyapunov exponent is large. This is illustrated by Fig. 6(c) which corresponds with the local peaks in the values of $\tilde{\lambda}_1$ and C_1 at $t \approx 89$ which is also indicated by the dashed line on the left in panels (a)-(b). Similarly, the leading order Lyapunov vector is spatially delocalized when the

instantaneous Lyapunov exponent is near a local minimum. An example of this is shown in Fig. 6(d) which corresponds to the dashed line on the right in panels (a)-(b) at $t \approx 97$.

Figure 7 illustrates the spatiotemporal dynamics of the 12th Lyapunov vector. This Lyapunov vector is of particular interest because it is the Lyapunov vector with a vanishing value of the Lyapunov exponent in our computations with $\lambda_{12} \approx 0$. A similar trend is found where the Lyapunov vector is more localized spatially when the instantaneous Lyapunov exponent is large and more delocalized when the instantaneous Lyapunov exponent is small. In addition, the time averaged value of C_{12} is smaller than for the leading order vector which indicates a smaller degree of spatial localization in comparison.

Figure 8 shows results for the 141st Lyapunov vector which represents a rapidly decaying vector. In this case, the results are quite different than what we found for the leading order and 12th Lyapunov vector. The instantaneous Lyapunov exponent has fluctuations at a higher frequency than before. In addition, the time averaged value of the localization is now quite small for all time where $C_{141}(t) \lesssim 1 \times 10^{-3}$. The spatial distribution of the Lyapunov vector now exhibits a checkered pattern for all time. Figure 8(c)-(d) shows that there is now little difference between the spatial patterns of the Lyapunov vector at the peaks and valleys of the localization.

In order to quantify the correlation between the localization and the instantaneous Lyapunov exponent we have also computed the equal-time cross-correlation $\langle \bar{C}_i(0)\bar{\lambda}_i(0) \rangle$ for all i. The quantities $\bar{C}_i(t)$ and $\bar{\lambda}_i(t)$ are simply the localization and the instantaneous Lyapunov exponent with their mean values subtracted off, respectively. Furthermore, the values plotted in Fig. 9 have been normalized by the equal-time cross-correlation for the leading order Lyapunov vector which had a value of 0.0024.

Figure 9 illustrates the variation of the cross-correlation for all of the covariant Lyapunov vectors. It is clear that there is a positive correlation which decreases as the index of the vector is increased. This is in agreement with the trends shown in Figs. 6-8. It is interesting to point out that the correlations are significantly larger for the covariant Lyapunov vectors with positive Lyapunov exponents ($i \leq 11$) which are shown as circles (blue). The decay in the positive correlations for these Lyapunov vectors decays more rapidly with increasing index i of the vector than those for $i \geq 12$ which are shown as squares (red).

Figure 10 shows a scatter-plot of the localization and instantaneous Lyapunov exponent for the data shown in Figs. 6-8. The circles (blue) are for $i = 1$, the squares (red) are for $i = 12$, and the triangles (green) are for $i = 141$. This clearly indicates that the leading order Lyapunov vector has values where the instantaneous Lyapunov exponent and localization are largest. The results for the 12th Lyapunov vector are similar but with small overall values. However, the results for the 141st Lya-

punov vector represent dynamics with uniformly much smaller values of the localization. Although we have focussed our attention on the results for $R = 5000$ in Figs. 6-9, we find similar trends over the entire range of Rayleigh numbers we have computed $5000 \leq R \leq 9000$.

Figures 6-8 suggest a decreasing trend in the localization of the Lyapunov vector as the index of the vector is increased. This is illustrated for all of the Lyapunov vectors we have computed in Fig. 11 where $\langle C_i \rangle_t$ is the time-average of C_i and i is the index of the Lyapunov vector. The time averaging was conducted using data over 100 time units.

Figure 11 clearly shows the decreasing trend in the average localization. Figure 11(a) shows results for $R = 5000$. The localization can be described by two linear regions. The circles (blue) represent the Lyapunov vectors where $\lambda_i > 0$ and the squares (red) represent the rest where $\lambda_i \leq 0$. The amount of localization is largest for the Lyapunov vectors with large positive values of the Lyapunov exponents and falls-off rapidly with the value of the index. The dashed-line is a linear curve fit through the circles (blue) with a slope of $\alpha_1 = -1.4 \times 10^{-4}$. The linear decay of the remaining vectors is shown by the dash-dotted line which has a slope of $\alpha_2 = -1.3 \times 10^{-5}$. Therefore $\alpha_1/\alpha_2 \approx 10$ indicating an order of magnitude faster fall-off in the localization of the Lyapunov vectors with positive exponents.

We have found the same trends for all of our simulations over the range of Rayleigh numbers $5000 \leq R \leq 9000$ as shown in Figure 11(b). For all of the Rayleigh numbers explored, the results yielded $\alpha_1 \approx -1 \times 10^{-4}$, $\alpha_2 \approx -1 \times 10^{-5}$, and so $\alpha_1/\alpha_2 \approx 10$. Although the distinction between the two regimes is not sharp, these results indicate that the spatial properties of the growing and decaying Lyapunov vectors are different.

C. Weighted Lyapunov vector

It would be very useful and insightful to be able to connect the spatial regions where the Lyapunov vector is large with the flow field dynamics. In most all previous studies on chaotic convection [27–31], only access to the leading order Lyapunov vector was possible. From information of the leading order Lyapunov vector the results suggested that small scale defects such as roll pinch-off events often resulted in regions of large Lyapunov vector. However, it was also shown that not all small defects and roll pinch-off events were significant in the sense of being located near a region of large magnitude of the leading order Lyapunov vector. In fact, Scheel and Cross [28] found that non-repeated defect events result in a more significant contribution to the leading order Lyapunov exponent than defect events that repeat in time.

In the following, we explore the possibility that the leading order Lyapunov vector only gives a partial picture of the dynamics. Using the covariant Lyapunov vectors it is possible to explore the possible connection between

the flow field and the Lyapunov vectors for the entire spectrum of vectors.

After experimenting with many different choices, we found that using a weighted Lyapunov vector for visualizing the Lyapunov vectors was the most effective approach. Using the results discussed in §III B we base the weighting scheme on the fact that the instantaneous Lyapunov exponents are largest when the Lyapunov vectors are highly localized. We define the weighted Lyapunov vector as

$$\vec{\xi}_w(x,y,t) = \sum_{i=1}^{N_w} e^{\tilde{\lambda}_i(t)\Delta t}|\delta T^{(i)}(x,y,z=1/2,t)| \qquad (12)$$

where N_w is the number of Lyapunov vectors to include in the weighting.

Essentially, this takes into account the spatial variations of all of the included Lyapunov vectors and weights their individual contribution using their value of the instantaneous Lyapunov exponent. It is important to recall that the instantaneous Lyapunov exponents fluctuate in time and that they are not guaranteed to maintain the strict ordering $\tilde{\lambda}_1(t) > \tilde{\lambda}_2(t) > \ldots$ for all time. Therefore, by using the weighting of Eq. (12) the significance of the different Lyapunov vectors is now a function of time. When a particular instantaneous Lyapunov exponent is at a local maximum, our previous results suggest that this Lyapunov vector will be localized, and by our weighting this Lyapunov vector will be given more weight.

Several examples of the weighted Lyapunov vector are shown in Fig. 12 for three different instances of time. Figure 12 presents a comparison between the leading order Lyapunov vector (left column containing panels (a), (c), (e)) and the weighted Lyapunov vector (right column containing panels (b), (d), (f)). The leading order Lyapunov vector is plotted as the absolute value of the temperature perturbation field at the mid-plane $|\delta T^{(1)}|$. The weighted Lyapunov vector is plotted using Eq. (12) with $N_w = 12$ which includes all of the Lyapunov vectors with non-negative Lyapunov exponents. The color contours represent the magnitude where red is large and blue is small values and the black lines indicate the convection rolls.

Figure 12(a)-(b) illustrates the typical situation where the leading order Lyapunov vector and the weighted Lyapunov vector are very similar in terms of their spatial variation. At this point in time there is a roll pinch-off event near the left side of the middle of the domain that is clearly picked up in panels (a) and (b). Similarly, in the upper left corner of the domain there is a wall-focus whose tip is about to merge with an adjacent convection roll which is also highlighted by both representations. This is often the case, and we have found that the leading order Lyapunov vector is usually a good indicator of the spatial locations where there are large divergences.

However, panels (c)-(d) and (e)-(f) of Fig. 12 provide good examples where the leading order Lyapunov vector is not a good indicator of what is represented by the weighted Lyapunov vectors. Panels (c)-(d) are for the same dynamics but at a later time where the leading order Lyapunov vector and the weighted Lyapunov vector are large in different regions of space. The leading order Lyapunov vector is large near the lower boundary which is only slightly noticeable in the weighted Lyapunov vector image.

More striking in these images is that the weighted Lyapunov vector is large near two defect structures that are not captured by the leading order Lyapunov vector. In particular, in Fig. 12(d) there is a roll pinch-off about to occur near the middle of the domain and a roll merger that is about to occur near the top of the domain. Both of these events do not yield regions of large magnitude in the leading order Lyapunov vector. A similar situation is illustrated in Fig. 12(e)-(f) where a roll pinch-off event has just recently occurred in the region justly slightly left of the center of the domain.

Before moving on we would like to say a few words on the choice of N_w. Figure 11 suggests that the Lyapunov vectors corresponding to the non-negative Lyapunov exponents are more localized and have a distinct fall-off in localization with increasing vector index. This is, in addition to the fact that they also have the largest expansion rates in the tangent space. For these reasons choosing N_w as the number of non-negative Lyapunov exponents was a natural choice.

However, we also explored the weighted Lyapunov vector for larger N_w. For larger N_w we found that the checkered pattern and the delocalization of the rapidly decaying Lyapunov vectors became more important. These effects eventually become strong enough to make it difficult to identify any particular region of space that is more important or distinct based upon its flow field pattern. Overall, we found that choosing N_w as the number of non-negative Lyapunov exponents to be the most insightful.

Overall, our results suggest that all of the Lyapunov vectors with positive Lyapunov exponents tend to be spatially localized with large magnitude near small scale defect structures such as convection roll pinch-offs and roll mergers. These small scale dynamics are often part of more complex defect interactions in the chaotic patterns we have explored that include targets, spirals, and dislocations.

However, not all of the small scale defects are represented as regions of large magnitude in any particular Lyapunov vector. In our results, we have found that the weighted Lyapunov vectors do show regions of large magnitude near all of the small scale defect structures. This suggests that these small scale structures are significant contributors to the overall disorder in the patterns. These results also open up the possibility of quantifying the relative importance of the different defects using the magnitude of the weighted Lyapunov vector. This is a subject of ongoing interest and future work.

IV. CONCLUSION

We have explored and quantified the spatiotemporal dynamics of the spectrum of covariant Lyapunov vectors of chaotic Rayleigh-Bénard convection. Although the chaotic dynamics we have investigated has a very high dimension in our finite computational representation (the dimension of our state-space is $\sim 6 \times 10^5$) we are now able to compute over 100 covariant Lyapunov vectors. We have shown that a much lower dimensional object, the thermal perturbation $\delta T^{(i)}$ at the horizontal mid-plane, is an accurate and useful representation of the spectrum covariant Lyapunov vectors.

We have used this to quantify the spatiotemporal dynamics of the Lyapunov vectors. In particular, we have quantified the spatial localization of the spectrum of Lyapunov vectors. We have found that the Lyapunov vectors are spatially localized when the instantaneous Lyapunov exponents are large. Furthermore, the Lyapunov vectors tend to be localized in regions containing topological defects in the flow field such as roll pinch-offs, dislocations, spiral structures, *etc.* This further suggests that defect features in the flow field play a significant role in the long-term predictability of the dynamics.

Our results suggest an interesting transition in the spatial localization of the Lyapunov vectors as the index of the vector increases. We find that the vectors which have positive Lyapunov exponents are more localized than the rest. In fact, there is an overall trend in the reduction of the spatial localization with increasing index where the fall-off is an order of magnitude faster for the Lyapunov vectors with positive exponents. The fact that the covariant Lyapunov vectors with positive Lyapunov exponents tend to be spatially localized near defect structures in the flow field further suggests the importance of the defects to the long-time dynamics. We have explored this further by investigating the spatial features of the weighted Lyapunov vector.

Overall, the ability to compute the covariant Lyapunov vectors for experimentally accessible fluid systems, such as Rayleigh-Bénard convection, provides an important window upon which to examine high-dimensional chaotic dynamics. We anticipate that the new physical insights gained using covariant Lyapunov vectors will continue to play an important role in building our understanding of the complex dynamics or large systems that are driven far-from-equilibrium.

[1] M. C. Cross and P. C. Hohenberg. Pattern formation outside of equilibrium. *Rev. of Mod. Phys.*, 65(3 II):851–1112, 1993.

[2] J. P. Gollub and J. S. Langer. Pattern formation in nonequilibrium physics. *Rev. Mod. Phys.*, 71(2):S396–S403, 1999.

[3] E. N. Lorenz. The predictability of a flow which possesses many scales of motion. *Tellus*, XXI(3):289–306, 1968.

[4] G. Ahlers. Turbulent convection. *Physics*, 2(74), 2009.

[5] M. J. Hoffman, N. S. LaVigne, S. T. Scorse, F. H. Fenton, and E. M. Cherry. Reconstructing three-dimensional reentrant cardiac electrical wave dynamics using data assimilation. *Chaos*, 26:013107, 2016.

[6] R. R. Kerswell. Recent progress in understanding the transition to turbulence in a pipe. *Nonlinearity*, 18(6):R17–R44, 2005.

[7] B. Hof, C. W. H. van Doorne, J. Westerweel, F. T. M. Nieuwstadt, H. Faisst, B. Eckhardt, H. Wedin, R. R. Kerswell, and F. Waleffe. Experimental observation of nonlinear traveling waves in turbulent pipe flow. *Science*, 305:1594–1598, 2004.

[8] D. Barkley. Theoretical perspective on the route to turbulence in a pipe. *J. Fluid Mech.*, 803:1–80, 2016.

[9] C. Castellano, S. Fortunato, and V. Loreto. Statistical physics of social dynamics. *Rev. Mod. Phys.*, 81:591–638, 2009.

[10] D. Ruelle. Ergodic theory of differentiable dynamical systems. *Publ. Math. IHES*, pages 275–306, 1979.

[11] D. Ruelle and J. P. Eckmann. Ergodic theory of chaos and strange attractors. *Rev. Mod. Phys.*, 57:617–656, 1985.

[12] P. V. Kuptsov and U. Parlitz. Theory and computation of covariant Lyapunov vectors. *J. Nonlinear Sci.*, 2012.

[13] F. Ginelli, H. Chatè, R. Livi, and A. Politi. Covariant Lyapunov vectors. *J. Phys. A: Math Theor.*, 46:1 – 25, 2013.

[14] F. Ginelli, P. Poggi, A. Turchi, H. Chatè, R. Livi, and A. Politi. Characterizing dynamics with covariant Lyapunov vectors. *Phys. Rev. Lett.*, 99:130601, 2007.

[15] C. L. Wolfe and R. M. Samelson. An efficient method for recovering Lyapunov vectors from singular vectors. *Tellus*, 59A:355–366, 2007.

[16] D. Pazó, I. G. Szendro, J. M. López, and M. A. Rodríguez. Structure of characteristic Lyapunov vectors in spatiotemporal chaos. *Phys. Rev. E*, 78:016209, 2008.

[17] H. Yang, K. A. Takeuchi, F. Ginelli, H. Chatè, and G. Radons. Hyperbolicity and the effective dimension of spatially extended dissipative systems. *Phys. Rev. Lett.*, 102:074102, 2009.

[18] E. Ott. *Chaos in dynamical systems*. Cambridge University Press, 1993.

[19] S. P. Kuznetsov. Dynamical chaos and uniformly hyperbolic attractors: from mathematics to physics. *Phys.-Usp.*, 54(2):119–144, 2011.

[20] S. P. Kuznetsov. *Hyperbolic chaos: a physicist's view.* Springer, 2012.

[21] M. Inubushi, M. U. Kobayashi, S. Takehiro, and M. Yamada. Covariant Lyapunov analysis of chaotic Kolmogorov flows. *Phys. Rev. E*, 85:016331, 2012.

[22] P. V. Kuptsov and U. Parlitz. Strict and fussy mode

splitting in the tangent space of the Ginzburg-Landau equation. *Phys. Rev. E*, 81:036214, 2010.

[23] K. A. Takeuchi, H. Yang, F. Ginelli, G. Radons, and H. Chatè. Hyperbolic decoupling of tangent space and effective dimension of dissipative systems. *Phys. Rev. E*, 84:046214, 2011.

[24] X. Ding, H. Chatè, P. Cvitanović, E. Siminios, and K. A. Takeuchi. Estimating the dimension of the inertial manifold from unstable periodic orbits. *Phys. Rev. Lett.*, 117:024101, 2016.

[25] X. Ding and P. Cvitanović. Periodic eigendecomposition and its application to Kuramoto-Sivashinsky system. *SIAM J. Appl. Dtn. Syst.*, 15(3):1434–1454, 2016.

[26] M. Xu and M. R. Paul. Covariant Lyapunov vectors of chaotic Rayleigh-Bénard convection. *Phys. Rev. E*, 93:062208, 2016.

[27] D. A. Egolf, I. V. Melnikov, W. Pesch, and R. E. Ecke. Mechanisms of extensive spatiotemporal chaos in Rayleigh-Bénard convection. *Nature*, 404:733–736, 2000.

[28] J. D. Scheel and M. C. Cross. Lyapunov exponents for small aspect ratio Rayleigh-Bénard convection. *Phys. Rev. E*, 74:066301, 2006.

[29] A. Jayaraman, J. D. Scheel, H. S. Greenside, and P. F. Fischer. Characterization of the domain chaos convection state by the largest Lyapunov exponent. *Phys. Rev. E*, 74:016209, 2006.

[30] M. R. Paul, M. I. Einarsson, P. F. Fischer, and M. C. Cross. Extensive chaos in Rayleigh-Bénard convection.

[31] A. Karimi and M. R. Paul. Quantifying spatiotemporal chaos in Rayleigh-Bénard convection. *Phys. Rev. E*, 85:046201, 2012.

[32] J. R. de Bruyn, E. Bodenschatz, S. W. Morris, D. S. Cannell, and G. Ahlers. Apparatus for the study of Rayleigh-Bénard convection in gases under pressure. *Rev. Sci. Instrum.*, 67(6):2043–2067, 1996.

[33] M. R. Paul, K.-H. Chiam, M. C. Cross, P. F. Fischer, and H. S. Greenside. Pattern formation and dynamics in Rayleigh-Bénard convection: numerical simulations of experimentally realistic geometries. *Physica D*, 184:114–126, 2003.

[34] S. Chandrasekhar. *Hydrodynamic and Hydromagnetic Stability.* Dover, New York, 1961.

[35] E. Bodenschatz, W. Pesch, and G. Ahlers. Recent developments in Rayleigh-Bénard convection. *Annu. Rev. Fluid Mech.*, 32:709–778, 2000.

[36] K-H. Chiam, M. Lai, and H. S Greenside. Efficient algorithm on a nonstaggered mesh for simulating Rayleigh-Bénard convection in a box. *Phys. Rev. E*, 68:026705, 2003.

[37] P. V. Kuptsov and S. P. Kuznetsov. Violation of hyperbolicity in a diffusive medium with local hyperbolic attractor. *Phys. Rev. E*, 80:016205, 2009.

[38] A. D. Mirlin. Statistics of energy levels and eigenfunctions is disordered systems. *Phys. Rep.*, 326:259–382, 2000.
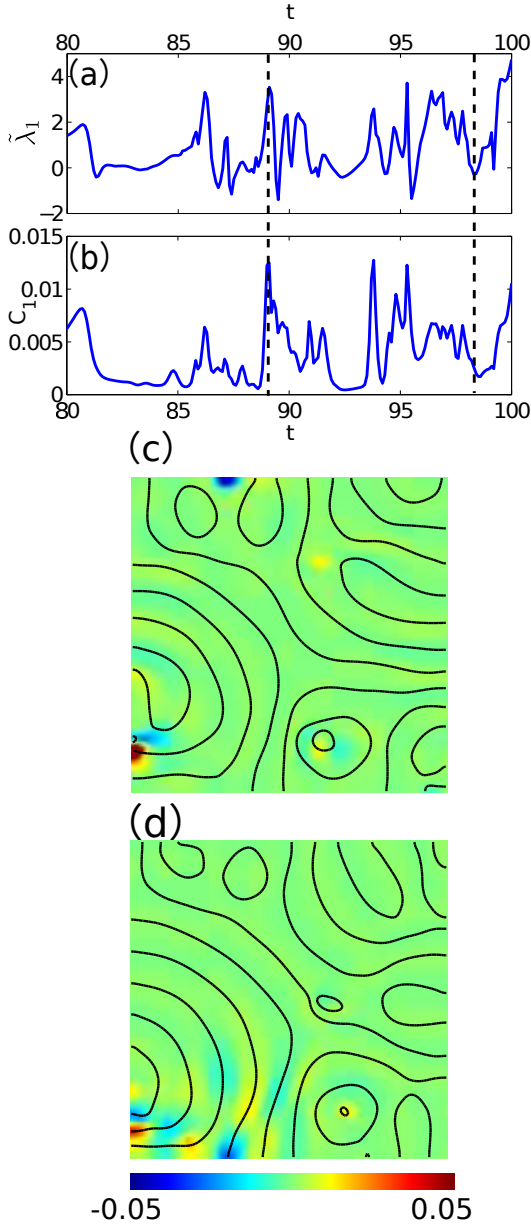
FIG. 6. (color online) (a) The time variation of the leading order instantaneous Lyapunov exponent $\tilde{\lambda}_1(t)$. (b) The time variation of the localization of the leading order Lyapunov vector $C_1(t)$. The vertical dashed line at $t = 89.3$ corresponds to the time when both $\tilde{\lambda}_1(t)$ and $C_1(t)$ exhibit a local peak in value. The spatial distribution of the Lyapunov vector for this case is shown in panel (c). The vertical dashed line at $t = 98.5$ corresponds to an instance when $\tilde{\lambda}_1(t)$ and $C_1(t)$ are at local a minimum. The Lyapunov vector at this time is shown in panel (d). Color contours indicate the value of the perturbation temperature $\delta T^{(i)}$ at the horizontal mid-plane ($z = 1/2$) where red is a large positive value and blue is a large negative value. The black solid lines indicate the location of the convection rolls. (Rayleigh number $R = 5000$, Prandtl number $\sigma = 1$, and aspect ratio $\Gamma = 16$).
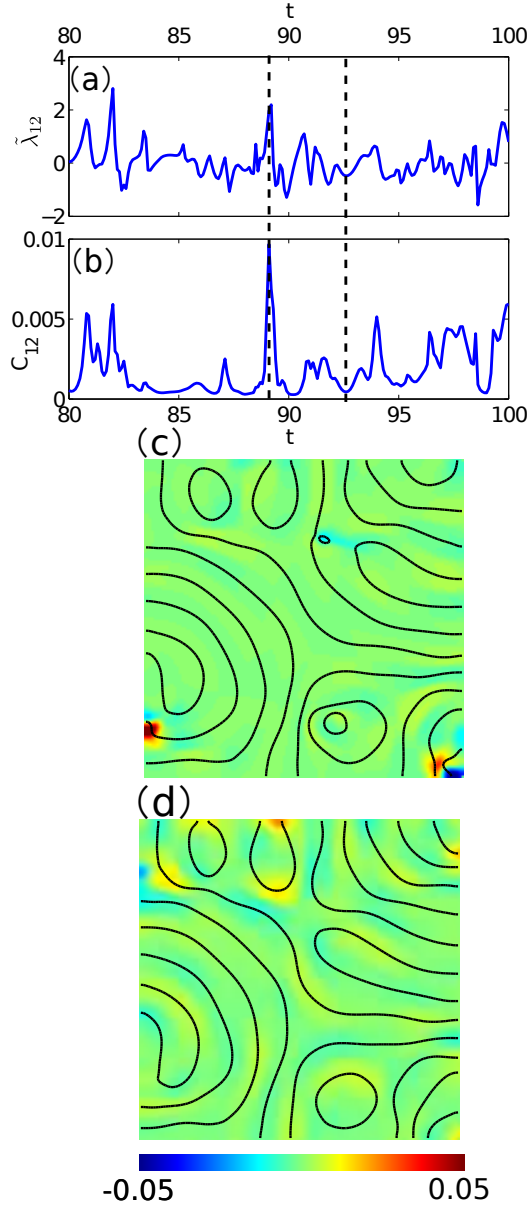
FIG. 7. (color online) The spatiotemporal features of the 12th Lyapunov vector where (a) shows the time variation of the instantaneous Lyapunov exponent $\tilde{\lambda}_{12}$, (b) shows the localization $C_{12}(t)$ and (c)-(d) show images of the Lyapunov vectors at times $t = 89$ and $t = 93$, respectively, which are also indicated by the vertical dashed lines. Simulation parameters and conventions are the same as Fig. 6.
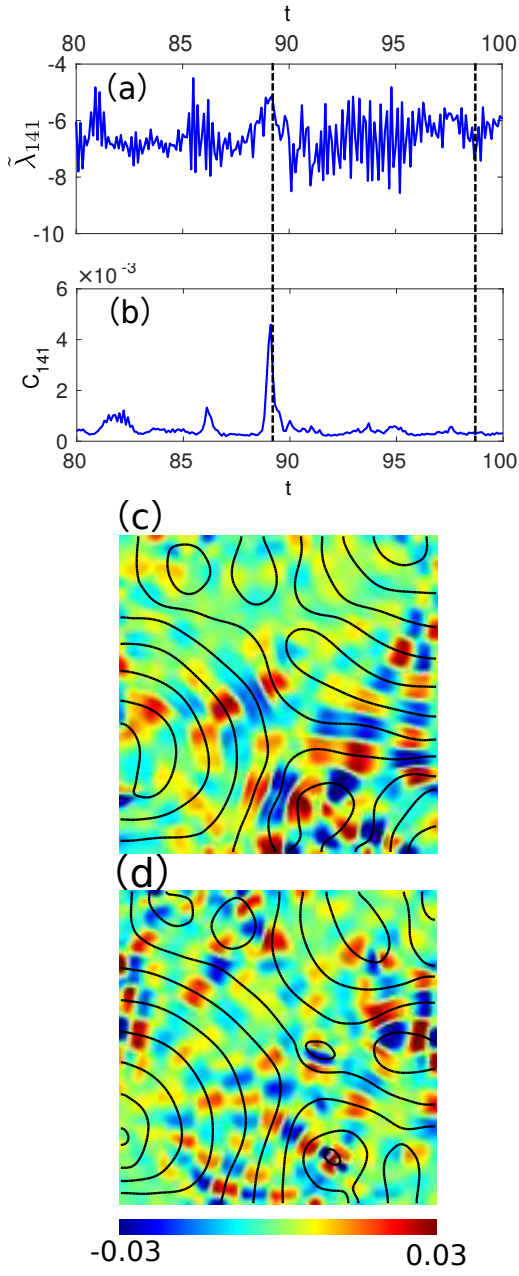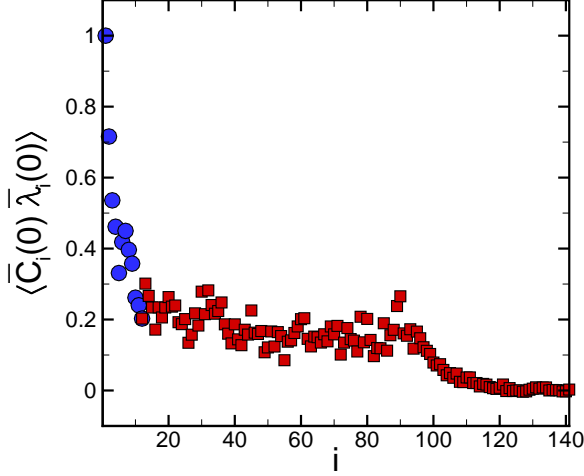
FIG. 8. (color online) The spatiotemporal features of the 141st Lyapunov vector where (a) shows the time variation of the instantaneous Lyapunov exponent $\tilde{\lambda}_{141}$, (b) shows the localization $C_{141}(t)$ and (c)-(d) show the Lyapunov vector at times $t = 89$ and $t = 98.5$, respectively, which are also indicated by the vertical dashed lines. Simulation parameters and conventions are the same as Fig. 6.

FIG. 9. (color online) The equal-time cross-correlation of the localization $C_i(t)$ and the instantaneous Lyapunov exponent $\tilde{\lambda}_i(t)$. The circles (blue) are for $i \leq 11$ which represent Lyapunov vectors with positive Lyapunov exponents $\lambda_i > 0$ and the squares (red) are for $i \geq 12$ which represent the Lyapunov vectors with $\lambda_i \leq 0$. The localization and the instantaneous Lyapunov exponent are positively correlated. The overall trend is a decreasing amount of correlation as i is increased. These results have been normalized by the value of the equal-time correlation computed for the leading order Lyapunov vector ($i = 1$) which had a value of 0.0024.
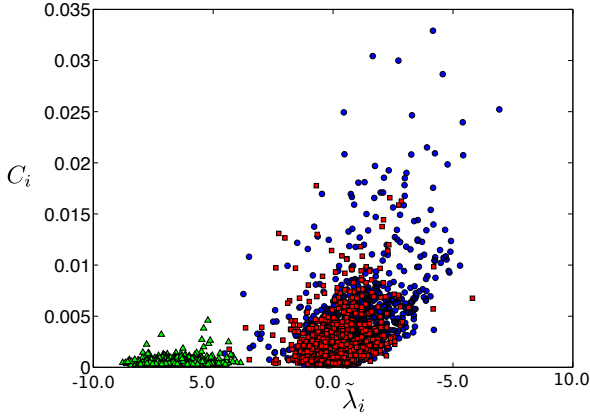

FIG. 10. (color online) The variation of the localization C_i with the instantaneous Lyapunov exponent $\tilde{\lambda}_i$. Circles (blue) are for the leading order Lyapunov vector, squares (red) are for the 12th covariant Lyapunov vector, and triangles (green) are for the 141st covariant Lyapunov vector.
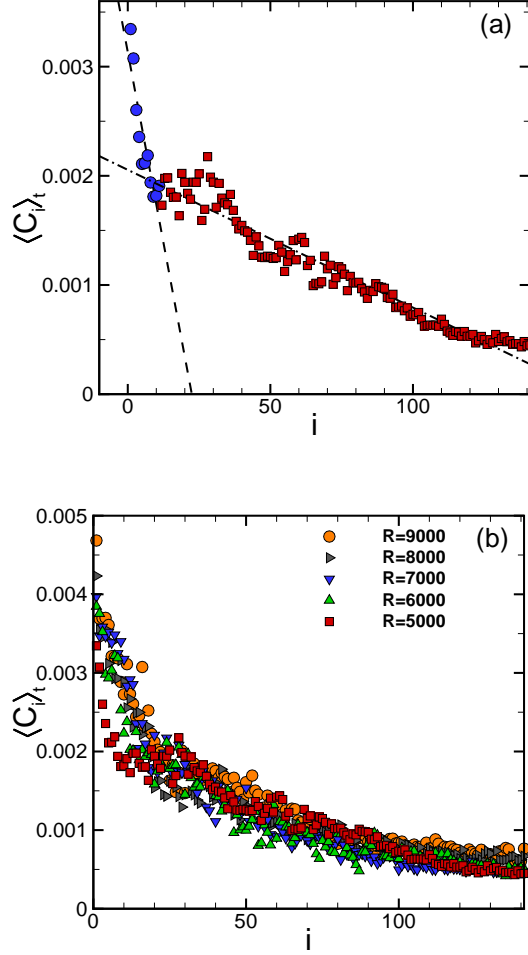
FIG. 11. (color online) The time average of the localization of the covariant Lyapunov vectors $\langle C_i \rangle_t$ where i is the index of the Lyapunov vector. The time average is taken over 100 time units. (a) Results for $R = 5000$ where the circles (blue) represent the first 11 Lyapunov exponents which are all positive. The squares (red) represent the remaining Lyapunov vectors which have Lyapunov exponents that are near zero or negative. The dashed line is a linear curve fit through the circles with slope $\alpha_1 = -1.6 \times 10^{-4}$. The dash-dotted line is a curve fit through the squares with slope $\alpha_2 = -1.3 \times 10^{-5}$. (b) Results for $5000 \leq R \leq 9000$. The overall trend is decreasing localization with increasing order of the Lyapunov vector. For all Rayleigh numbers, the localization of the Lyapunov vectors associated with positive exponents falls off approximately 10 times faster than the localization of the remaining vectors with increasing order i.
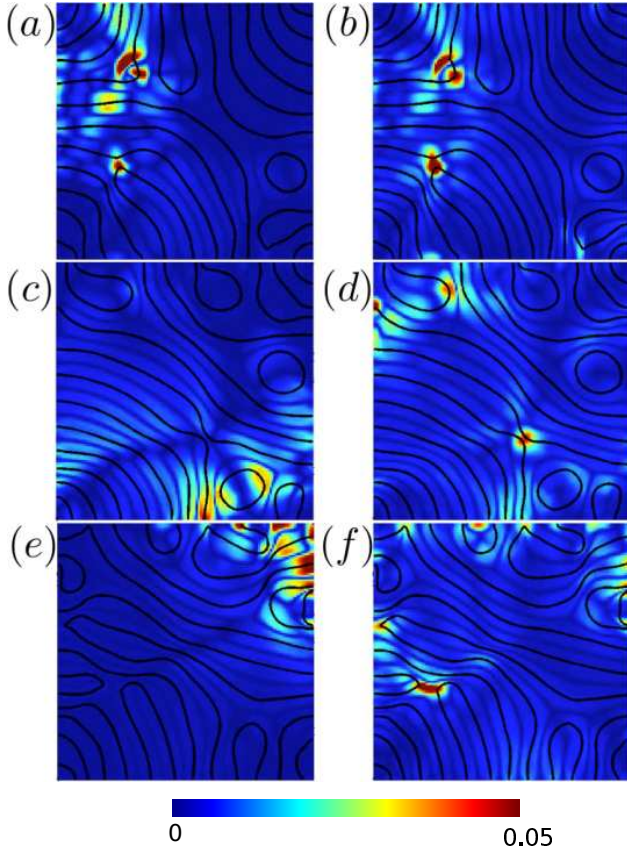
FIG. 12. (color online) Comparison of the spatial variation of the leading order Lyapunov vector and the weighted covariant Lyapunov vector. Color represents the magnitude of the Lyapunov vector where red is large and blue is small. The black contour lines indicate the boundaries of the convection rolls. Each row shows results at at different instant of time where the left side, panels (a), (c), (e), illustrate the leading order Lyapunov vector and the right side, panels (b), (d), (f), represent the weighted Lyapunov vectors.